Bandstructure Engineering by Surface Water Dosing on $SrFe_2As_2$

Y. M. Zhang(张昱萌)[1,2], F. Wu(吴凡)[1,3], W. J. Shi(史武军)[1,4], Z. A. Xu(许志安)[1], S. C. Shi(石书丞)[1], G. Y. He(何冠阳)[1], C. Chen(陈成)[1], H. F. Yang(杨海峰)[1], L. X. Yang(杨乐仙)[5], Z. Liu(刘志)[1,4], W. Lu(陆卫)[1,2,6], Y. Zhang(张焱)[7], Y. F. Guo(郭艳峰)[1*], Y. L. Chen(陈宇林)[1,8*], and Z. K. Liu(柳仲楷)[1*]

[1]School of Physical Science and Technology, ShanghaiTech Laboratory for Topological Physics, ShanghaiTech University, Shanghai 201210, China

[2]Zhangjiang Laboratory, 100 Haike Road, Pudong, Shanghai 201210, China

[3]Lingang Laboratory, Shanghai,200031, China

[4]Center for Transformative Science, ShanghaiTech University, Shanghai 201210, China

[5]State Key Laboratory of Low Dimensional Quantum Physics, Department of Physics, Tsinghua University, Beijing, 100084, China

[6]State Key Laboratory of Infrared Physics, Shanghai Institute of Technical Physics, Chinese Academy of Sciences, 500 Yu-Tian Road, Shanghai 200083, China

[7]International Center for Quantum Materials, Peking University, Beijing, 100871, China

[8]Department of Physics, Clarendon Laboratory, University of Oxford, Parks Road, Oxford OX1 3PU, UK

[*]Corresponding authors. E-mails: guoyf@shanghaitech.edu.cn; chenyl1@shanghaitech.edu.cn; liuzhk@shanghaitech.edu.cn.

Abstract

Fe-based superconductors represent a fascinating class of materials, extensively studied for their complex interplay of superconductivity, magnetism, spin density waves, and nematicity, along with the interactions among these orders. An intriguing and yet unexplained phenomenon observed in Fe-based superconductors is the emergence of superconductivity below 25K in the non-superconducting parent compound $SrFe_2As_2$ following exposure to water at its surface. In this study, we employed in-situ angle-resolved photoemission spectroscopy and low-energy electron diffraction to meticulously examine the electronic structure evolution of $SrFe_2As_2$ upon in-situ water dosing. Our findings indicate that water dosing markedly attenuates the SDW phase and surface Sr reconstruction, yet preserves the nematic order in the $SrFe_2As_2$. Furthermore, we detected an enhancement in the spectral weight of bands near the Fermi level. Our observations highlight the critical role of the intricate interplay among various orders induced by water dosing, which effectively modifies the band structure and favor the emergence of superconductivity in $SrFe_2As_2$.

I. Introduction

In the last decade, iron-based superconductors (FeSCs) have emerged as a pivotal subject of study for their role in elucidating unconventional superconductivity. The intricate interplay among their electronic, structural, and spin degrees of freedom gives rise to phenomena such as quantum criticality, superconductivity, and non-Fermi liquid behavior [1–5], leading to complex phase diagrams [6–9].

Among the iron-based superconductors, the 122-family member $SrFe_2As_2$ exhibits several characteristics common to other 122 compounds. Like its counterparts, it possesses a non-superconducting parent compound phase and undergoes structural and spin density wave (SDW) transitions upon cooling [10–17]. Superconductivity can be induced in $SrFe_2As_2$ via carrier doping through aliovalent ion substitution or by the application of high pressure, both of which suppress these structural and magnetic transitions [18–26]. Furthermore, $SrFe_2As_2$ displays a 2×1 surface reconstruction of Sr atoms following vacuum cleaving, a phenomenon that may also occur in other 122 compounds [27,28]. In contrast, $SrFe_2As_2$ is distinguished by a particularly strong coupling between the SDW transition and structural distortion, setting it apart from other members of the 122 family [16,29].

An intriguing phenomenon of $SrFe_2As_2$ is the reported emergence of superconductivity in thin films exposed to water vapor, with a transition temperature (Tc) of 25K [30]. Similar water induced superconductivity is also reported in other FeSCs (e.g. $FeTe_{1-x}S_x$ [31,32]). Unlike other water induced superconducting systems (such as Na_xCoO_2), where two-dimensionality is boosted [33–35], DFT calculations and the X-ray diffraction data of $SrFe_2As_2$ suggest the decrease of the interlayer distance with water dosing [36,30]. Such deviation indicates a unique mechanism for superconductivity may exist in water dosed $SrFe_2As_2$. Currently, the spectroscopic signature detailing the evolution of electronic and surface structures following water exposure remains elusive, leaving the fundamental mechanisms driving the onset of superconductivity unexplored.

This study delves into the changes in the surface and electronic structures of $SrFe_2As_2$ following in situ water dosing, utilizing low energy electron diffraction (LEED) and angle-resolved photoemission spectroscopy (ARPES). Our findings demonstrate the disappearance of the SDW and Sr surface reconstruction post water dosing, while the nematic order persists. Additionally, we observed an enhancement in the spectral weight of bands near the Fermi level, indicating increased metallicity. These results suggest that the suppression of competing orders (SDW and Sr reconstruction) and the survival of nematicity together boosts the metallicity, potentially playing a crucial role in the emergence of superconductivity in water-dosed $SrFe_2As_2$. We propose that the charge transfer from water molecules, evidenced by the ambient pressure X-ray photoelectron spectroscopy (APXPS) measurements might drive such bandstructure evolution.

II. Results

The crystal structure of $SrFe_2As_2$ at room temperature is shown in Fig. 1a, showing a tetragonal structure with Sr atoms between Fe-As planes. At lower temperature, $SrFe_2As_2$ exhibits three distinct orders as illustrated in Fig. 1b: a transition from tetragonal to orthorhombic lattice distortion below 190K, the emergence of a SDW phase also below 190K, and the reconstruction of surface Sr atoms [27]. LEED measurements on cleaved sample surfaces distinctly show Bragg spots at room temperature (300K) and, at lower temperatures (80K), additional diffraction spots attributable to 2×1 and 1×2 Sr atom surface reconstructions (we note the large electron beam spot covers both 1×2 and 2×1 Sr surface reconstruction regions), alongside $\sqrt{2} \times \sqrt{2}$ SDW ordering. The tetragonal to orthorhombic distortion has small effect on the Bragg peak positions and could not be observed from the LEED measurement. These findings align with prior studies [27,37].

The emergence of these orders in $SrFe_2As_2$ leads to significant rearrangements within its electronic band structure, which can be effectively probed using ARPES. In $SrFe_2As_2$, the band structure near the Fermi level is dominated by the 3d orbitals of Fe arranged by the crystal field splitting. At low temperatures, the band structure undergoes several modifications: nematic splitting which results in distinct energy shifts for the d_{xz} and d_{yz} orbitals [38]; $\sqrt{2} \times \sqrt{2}$ SDW reconstruction evident by the band folding between $\bar{\Gamma}$ and $\bar{\mathrm{M}}$ along the (π/2, π/2) direction; and 2×1 Sr surface reconstruction, observable through band folding between $\bar{\Gamma}$ and $\bar{\mathrm{X}}$ along the (π,0) direction. These modifications collectively result in Brillouin zone folding and shape the intricate reconstructed band structure depicted in Fig. 1c. As will be discussed further, surface exposure to water mitigates the effects of SDW and Sr surface reconstruction while preserving the nematic splitting, thereby creating a new band structure favoring superconductivity.

The methodology and setup for the in-situ water dosing experiment are elaborated in the methods section and Supplemantary Note 1, respectively. The sample is cleaved in vacuum for LEED and ARPES measurements. Subsequent to each water exposure, both the LEED pattern and the ARPES spectra are recorded to monitor the changes in the surface structure and electronic bandstructure. Fig. 2 illustrates the LEED patterns and the evolution of the diffraction spots observed after water dosing. It is evident that, despite the persistence of the Bragg spots following four consecutive water dosages, the other diffraction spots attributable to the $\sqrt{2} \times \sqrt{2}$ SDW reconstruction as well as 2×1 Sr surface reconstruction are progressively diminished and ultimately vanish.

To better visualize the relative spot intensity, line profiles were extracted from the LEED image, traversing the diffraction spots as depicted in Fig. 2g-h. The analysis reveals that the intensity of all three types of peaks diminishes following water exposure due to the degraded sample surface. Notably, the intensities associated with both the Sr surface and SDW reconstructions exhibit a markedly accelerated decline, as demonstrated by the plot contrasting the relative intensities of the reconstruction and Bragg peaks (Fig. 2i). Upon the application of four water dosages, the relative intensity approaches near-zero levels, similar to the high temperature LEED results.

In-situ ARPES measurements on the water dosed sample systematically reveal the evolution of the electronic structure, further proving the disappearance of SDW and Sr surface reconstruction from the electronic band structure aspect (Fig. 3-5 and Supplemantary Note 2). Fig. 3a-c plots the photoemission intensity along the $\bar{\Gamma} - \bar{\mathrm{X}}$ direction after water dosage. From the spectrum in the pristine sample surface, we could see clear band dispersion around the $\bar{\Gamma}$ point and much weaker dispersions around the $\bar{X}$ point as surrounded by a rectangular box in Fig. 3a. The band dispersions around $\bar{X}$ are replicas of $\bar{\Gamma}$ bands due to the $\bar{\Gamma}-\bar{X}$ band folding induced by the 2×1 Sr surface reconstruction [28]. After water dosage, the band dispersion around the $\bar{\Gamma}$ point remains largely unaffected, whereas the intensity around the $\bar{X}$ point is gradually suppressed. The suppression effect on the replica bands is more discernibly captured through the energy distribution curve (EDC) at the $\bar{X}$ point (Fig. 3d), where the attenuated bands, marked by arrows and further elaborated post-linear background subtraction, correspond to the EDC peaks. Quantitative assessment of these EDC peak spectral weights reveals a decrease with successive water dosage. After three water dosages, the intensity almost drops to zero, indicating the complete suppression of the reconstructed bands and consistent with LEED observations.

Fig. 4 illustrates the evolution of band dispersion along the $\bar{\Gamma}-\bar{M}$ direction in response to water dosage. Along the $\bar{\Gamma}-\bar{M}$ direction, the high temperature band structure of pristine $SrFe_2As_2$ goes through modifications including nematic splitting, SDW-induced folding and gap formation and forms the low temperature band structure, as depicted in the schematic of Fig. 4a (with detailed discussions available in references [39,40]). The ARPES spectrum acquired along this direction (Fig. 4b) well captures the anticipated band structure shown in the schematic: Near the $\bar{\Gamma}$ point, the α, β_1, β_2 bands are the hole-like bands, whereas the γ' band, an electron-like band folded from the $\bar{M}$ point, is apparent. The β_1, β_2 bands originate from the nematic splitting of the d_{xz} and d_{yz} orbitals, with the observed pair corresponding to the twinned domain contributions [38]. Near the $\bar{M}$ point, the presence of hole-like α, β_2' and η bands as well as the electron-like γ band is noted. The γ' and β_2 band, γ and β_2' band crosses near the $\bar{\Gamma}$ and $\bar{M}$ point respectively and form SDW gaps. These band crossings typically yield Dirac points along high-symmetry lines; however, slight misalignments in the experimental setup allows us to observe band gaps instead (refer to [38] for more details). The complex band structure along the $\bar{\Gamma}-\bar{M}$ direction underscores the influence of nematicity and SDW ordering on the electronic properties of $SrFe_2As_2$.

Upon water dosing, we observed the gradual disappearing of the γ' band and the associated band crossings between γ' and β_2, and between γ and β_2' band. The disappearing of the folded bands further leads to the closing of the SDW gap, as indicated by the arrows in Fig. 4c. Beyond the dissolution of SDW ordering, the band structure undergoes additional changes, notably the shifting of the α, β_2, and η towards the Fermi level. This trend hints at the introduction of hole-doping by water, as elaborated in the Fig. S4,5 [41]. Despite these modifications, the splitting between β_1 and β_2 persists after all the water dosages, suggesting the survival of nematic order. Furthermore, water dosing appears to enhance the anisotropy of the Fermi surface around the $\bar{M}$ point along the k_x and k_y axes, highlighting the different doping effect on d_{yz} and d_{xy} orbitals [39] (See Fig. S6 for details).

Despite witnessing various band evolutions, the emergence of a superconducting gap after water dosage remains elusive, possibly due to inadequate water dosage. A higher water volume might promote superconductivity, yet it concurrently degrades the surface quality, adversely affecting ARPES measurement. However, we observe an increase in the spectral weight of $SrFe_2As_2$, including that of the quasiparticle peak near the Fermi level along $\bar{\Gamma}-\bar{X}$ direction after water dosing, indicating enhanced metallicity. Fig. 5 illustrates the band dispersions near the Fermi surface along the high-symmetry $\bar{\Gamma'}-\bar{M}-\bar{\Gamma''}$, $\bar{\Gamma}-\bar{M}$, $\bar{\Gamma}-\bar{X}$ directions (referenced in the constant energy contour in the Fermi energy in Fig. 5a), both pre- and post-water dosage. To highlight the spectral weight difference, EDCs for the β and γ bands (labeled by the orange and blue arrows in Fig. 5b, c, d) at the Fermi momentum along these directions are elaborated to trace the spectral weight evolution of the EDCs in response to water dosing. This examination reveals a notable increase including the quasiparticle spectral weight of these bands. We note the Fermi momentum of these bands is different from the momentum positions associated with SDW gap formation, implying that the spectral weight enhancement is not a consequence of SDW gap closure. This observation indicates an enhanced metallicity, a remarkable outcome for surface dosing experiments where an increase in adsorbates typically leads to a reduction in spectral weight on the surface. Consistent evidence is also provided by STM measurements, including the increase of quasiparticle spectral weight near E_F and the emergence of a V-shape gap structure typical of Fe-based superconductors (see Supplementary Note 3 and Fig. S9).

III. Discussion

Our experimental findings reveal significant modifications in the electronic structure of $SrFe_2As_2$ with water dosage, including the suppression of the SDW order and the surface reconstruction, the persistence of nematicity, and an increase in spectral weight near the Fermi level, all of which could potentially facilitate the emergence of superconductivity. The underlying mechanisms driving these notable changes remain to be fully elucidated. One plausible explanation is that water dosing induces effective hole doping, which triggers a phase transition in $SrFe_2As_2$, as indicated by the phase diagram (see Fig. S5) and supported by referenced studies [42–47]. The level of hole doping, inferred from our measurements, suggests that each water dosage introduces approximately 0.116 holes per unit cell ($7.56 \times 10^{13}/\mathrm{cm}^2$), as detailed in the Supplementary Information Note 2 and Fig. S5, sufficient to suppress SDW ordering and enhance metallicity. The APXPS experiment also provides evidence of electron transfer from the sample to water molecules, indicating a tendency of p-type doping in the sample (See Supplemantary Note 4 and Fig. S10). Further investigations into the water-incorporated crystal structure indicate that in the most stable configuration, 0.034644 electrons per water molecule are transferred from the $SrFe_2As_2$ surface to the water molecules (Fig. S11). Beyond electron transfer, surface reconstructions may also play a pivotal role in the evolution of the electronic structure. However, such reconstructions have not been detected in LEED and ARPES analyses and call for evidences from additional surface-sensitive experimental techniques.

IV. Conclusion

In summary, we systematically investigated the impact of water dosing on the electronic structure of $SrFe_2As_2$, revealing a series of significant alterations: the diminution of SDW order and surface reconstructions, the endurance of nematic order, and a pronounced increase in spectral weight near the Fermi level, which collectively promote superconductivity. Our experimental and computation analysis suggest that the electron transfer could be key in the observed evolution of the electronic structure. These insights open new avenues for understanding the interplay between surface chemistry, complex orders and electronic properties in iron-based superconductors, highlighting the potential of surface treatments in tuning their physical properties.

V. Methods

ARPES and LEED experiments

ARPES experiments were performed at the home-built ARPES setup in ShanghaiTech University, where samples were cleaved in situ and measured under high vacuum conditions of greater than 5×10^{-10} Torr. The instrument was equipped with a Scienta DA30 electron energy analyzer, and helium lamp as the light source with a photon energy of 21.2 eV. The experiments were all performed around 20 K or 80K. The ARPES chamber is equipped with an in-situ LEED setup for measuring the surface orders. The LEED image for $SrFe_2As_2$(001) surface obtained for an energy of 113eV and at low temperature around 80K, high temperature around 300K.

Surface water dosing

The ARPES measurement chamber is equipped with an in-situ water dosing setup as shown in the Fig. S1. High purity water vapor is generated from evaporation of de-ionized water stored in the glass test tube and introduced into the vacuum chamber through pipelines, a leak valve and a capillary. The capillary would generate high density water vapor without damaging the chamber vacuum. Each dosing round lasts for about 6-8 seconds while the vacuum level is kept below 5×10^{-10} Torr.

STM experiments

The STM and STS measurements were performed under ultrahigh vacuum (pressure $\leq 1\times 10^{-11}$ mbar) at 4.3K on the Unisoku JT-STM, with PtIr scanning tip. The constant-height dI/dV spectroscopy was acquired by turning off the feedback loop and using the standard lock-in techniques (f = 991.7 Hz, V_{ampl}= 4 mV). The tip was calibrated on Ag (111) before measurements on the samples.

APXPS experiments

APXPS measurements were carried out at BL02B01, the Shanghai Synchrotron Radiation Facility. The samples were cleaved in situ and measured under high vacuum conditions of greater than 1×10^{-9} Torr. The water vapor was dosed in succession and held until the pressure of analysis chamber kept stable. Unless otherwise stated, the spectra were fitted by Casa XPS software using a Shirly-type background. The symmetrical peaks were fitted using the GL (30) line shape (a mixing of 70% Gaussian and 30% Lorentzian).

Computation Methods

The first-principles calculations were performed using the Vienna ab initio Simulation Package (VASP) [48]. The interactions between the valence electrons and ion cores are described by the projector augmented wave method [49,50], and exchange-correlation potential was formulated by the generalized gradient approximation with the Perdew-Burke-Ernzerhof (PBE) scheme [51]. A slab model of 2 cells separated by 20 Å vacuum was employed. To simulate the water molecular adsorption on surface, a 3×3 supercell with one water molecular adsorpted on the As-terminated surface was used, where the distance between two water molecular was larger than 10 Å. The Γ-centered 4×4×1 k-points were used for the first Brillouin-zone (BZ) sampling. The kinetic energy cutoff was set to 536 eV. The initial molecular at top, bridge, and hollow position was employed. And the structures were relaxed until the forece is less than 0.05 eV/Å.

VI. Acknowledgments

Z. K. Liu acknowledges the support from the National Nature Science Foundation of China (92365204, 12274298) and the National Key R&D program of China (Grant No. 2022YFA1604400/03). Y. M. Zhang acknowledges the support from Zhangjiang Laboratory. The authors thank BL02B at the Shanghai Synchrotron Radiation Facility supported by National Natural Science Foundation of China under contract no. 11227902.

References

[1] P. Richard, T. Sato, K. Nakayama, T. Takahashi, and H. Ding, Fe-based superconductors: an angle-resolved photoemission spectroscopy perspective, *Rep. Prog. Phys.* **74**, 124512 (2011).

[2] P. J. Hirschfeld, M. M. Korshunov, and I. I. Mazin, Gap symmetry and structure of Fe-based superconductors, *Rep. Prog. Phys.* **74**, 124508 (2011).

[3] G. R. Stewart, Superconductivity in iron compounds, *Rev. Mod. Phys.* **83**, 1589 (2011).

[4] E. Abrahams and Q. Si, Quantum criticality in the iron pnictides and chalcogenides, *J. Phys. Condens. Matter* **23**, 223201 (2011).

[5] J. Paglione and R. L. Greene, High-temperature superconductivity in iron-based materials, *Nat. Phys.* **6**, 645 (2010).

[6] Q. Si and E. Abrahams, Strong Correlations and Magnetic Frustration in the High T_c Iron Pnictides, *Phys. Rev. Lett.* **101**, 076401 (2008).

[7] J. Wu, P. Phillips, and A. H. Castro Neto, Theory of the Magnetic Moment in Iron Pnictides, *Phys. Rev. Lett.* **101**, 126401 (2008).

[8] R. M. Fernandes, A. V. Chubukov, and J. Schmalian, What drives nematic order in iron-based superconductors?, *Nat. Phys.* **10**, 2 (2014).

[9] N. J. McLaughlin et al., Strong Correlation Between Superconductivity and Ferromagnetism in an Fe-Chalcogenide Superconductor, *Nano Lett.* **21**, 7277 (2021).

[10] Q. Huang, Y. Qiu, W. Bao, M. A. Green, J. W. Lynn, Y. C. Gasparovic, T. Wu, G. Wu, and X. H. Chen, Neutron-Diffraction Measurements of Magnetic Order and a Structural Transition in the Parent $BaFe_2As_2$ Compound of FeAs-Based High-Temperature Superconductors, *Phys. Rev. Lett.* **101**, 257003 (2008).

[11] R. M. Fernandes and O. Vafek, Distinguishing spin-orbit coupling and nematic order in the electronic spectrum of iron-based superconductors, *Phys. Rev. B* **90**, 214514 (2014).

[12] W. Z. Hu, J. Dong, G. Li, Z. Li, P. Zheng, G. F. Chen, J. L. Luo, and N. L. Wang, Origin of the Spin Density Wave Instability in AFe_2As_2 (A = Ba, Sr) as Revealed by Optical Spectroscopy, *Phys. Rev. Lett.* **101**, 257005 (2008).

[13] M. Yi et al., Unconventional electronic reconstruction in undoped (Ba, Sr)Fe_2As_2 across the spin density wave transition, *Phys. Rev. B* **80**, 174510 (2009).

[14] X. Liu, R. Tao, M. Ren, W. Chen, Q. Yao, T. Wolf, Y. Yan, T. Zhang, and D. Feng, Evidence of nematic order and nodal superconducting gap along [110] direction in $RbFe_2As_2$, *Nat. Commun.* **10**, 1039 (2019).

[15] L. X. Yang et al., Electronic Structure and Unusual Exchange Splitting in the Spin-Density-Wave State of the $BaFe_2As_2$ Parent Compound of Iron-Based Superconductors, *Phys. Rev. Lett.* **102**, 107002 (2009).

[16] J. Zhao, W. Ratcliff II, J. W. Lynn, G. F. Chen, J. L. Luo, N. L. Wang, J. Hu, and P. Dai, Spin and Lattice Structure of Single Crystal $SrFe_2As_2$, *Phys. Rev. B* **78**, 140504 (2008).

[17] B. Zhou et al., High-resolution angle-resolved photoemission spectroscopy study of the electronic structure of $EuFe_2As_2$, *Phys. Rev. B* **81**, 155124 (2010).

[18] M. Yi et al., Dynamic competition between spin-density wave order and

superconductivity in underdoped $Ba_{1-x}K_xFe_2As_2$, *Nat. Commun.* **5**, 3711 (2014).

[19] Y. Zhang, Z. R. Ye, Q. Q. Ge, F. Chen, J. Jiang, M. Xu, B. P. Xie, and D. L. Feng, Nodal superconducting-gap structure in ferropnictide superconductor $BaFe_2(As_{0.7}P_{0.3})_2$, *Nat. Phys.* **8**, 371 (2012).

[20] T. Sato et al., Band Structure and Fermi Surface of an Extremely Overdoped Iron-Based Superconductor KFe_2As_2, *Phys. Rev. Lett.* **103**, 047002 (2009).

[21] S. R. Saha, N. P. Butch, K. Kirshenbaum, and J. Paglione, Evolution of bulk superconductivity in $SrFe_2As_2$ with Ni substitution, *Phys. Rev. B* **79**, 224519 (2009).

[22] Y. Zhang et al., Unusual Doping Dependence of the Electronic Structure and Coexistence of Spin-Density-Wave and Superconductor Phases in Single Crystalline $Sr_{1-x}K_xFe_2As_2$, *Phys. Rev. Lett.* **102**, 127003 (2009).

[23] W. O. Uhoya, J. M. Montgomery, G. M. Tsoi, Y. K. Vohra, M. A. McGuire, A. S. Sefat, B. C. Sales, and S. T. Weir, Phase transition and superconductivity of $SrFe_2As_2$ under high pressure, *J. Phys. Condens. Matter* **23**, 122201 (2011).

[24] V. B. Zabolotnyy et al., (π, π) electronic order in iron arsenide superconductors, *Nature* **457**, 569 (2009).

[25] B. A. Frandsen et al., Local orthorhombicity in the magnetic C_4 phase of the hole-doped iron-arsenide superconductor $Sr_{1-x}Na_xFe_2As_2$, *Phys. Rev. Lett.* **119**, 187001 (2017).

[26] S. R. Saha, N. P. Butch, K. Kirshenbaum, and J. Paglione, Superconducting and ferromagnetic phases induced by lattice distortions in $SrFe_2As_2$, *Phys. Rev. Lett.* **103**, 037005 (2009).

[27] F. C. Niestemski, V. B. Nascimento, B. Hu, W. Plummer, J. Gillett, S. Sebastian, Z. Wang, and V. Madhavan, Unveiling the Atomic and Electronic Structure at the Surface of the Parent Pnictide $SrFe_2As_2$, arXiv:0906.2761.

[28] D. Hsieh, Y. Xia, L. Wray, D. Qian, K. Gomes, A. Yazdani, G. F. Chen, J. L. Luo, N. L. Wang, and M. Z. Hasan, Experimental Determination of the Microscopic Origin of Magnetism in Parent Iron Pnictides, arXiv:0812.2289.

[29] J. J. Wu, J. F. Lin, X. C. Wang, Q. Q. Liu, J. L. Zhu, Y. M. Xiao, P. Chow, and C. Q. Jin, Magnetic and structural transitions of $SrFe_2As_2$ at high pressure and low temperature, *Sci. Rep.* **4**, 1 (2014).

[30] H. Hiramatsu, T. Katase, T. Kamiya, M. Hirano, and H. Hosono, Water-induced superconductivity in $SrFe_2As_2$, *Phys. Rev. B* **80**, 052501 (2009).

[31] Y. Mizuguchi, K. Deguchi, S. Tsuda, T. Yamaguchi, and Y. Takano, Moisture-induced superconductivity in $FeTe_{0.8}S_{0.2}$, *Phys. Rev. B* **81**, 214510 (2010).

[32] K. Deguchi, Y. Mizuguchi, Y. Kawasaki, T. Ozaki, S. Tsuda, T. Yamaguchi, and Y. Takano, Alcoholic beverages induce superconductivity in $FeTe_{1-x}S_x$, *Supercond. Sci. Technol.* **24**, 055008 (2011).

[33] N. Katayama, M. Nohara, F. Sakai, and H. Takagi, Enhanced Superconducting Transition Temperature in the Water-intercalated Sulfides, *J. Phys. Soc. Jpn.* **74**, (2005).

[34] A. Lerf and F. Sernetz, Superconductivity in Layered Ternary Chalcogenides A_xTaS_2 and A_xNbS_2 and Influence of Topotactic Solvation, *Mat.Res.Bull* **14**, 797 (1979).

[35] K. Takada, H. Sakurai, E. Takayama-Muromachi, F. Izumi, R. A. Dilanian, and T.

Sasaki, Superconductivity in two-dimensional CoO_2 layers, *Nature* **422**, 53 (2003).

[36] T. Kamiya, H. Hiramatsu, T. Katase, M. Hirano, and H. Hosono, Impurities in FeAs-based superconductor, $SrFe_2As_2$, studied by first-principles calculations, *Mater. Sci. Eng. B* **173**, 244 (2010).

[37] V. B. Nascimento et al., Surface Geometric and Electronic Structures of $BaFe_2As_2(001)$, *Phys. Rev. Lett.* **103**, 076104 (2009).

[38] M. Yi et al., Symmetry-breaking orbital anisotropy observed for detwinned $Ba(Fe_{1-x}Co_x)_2As_2$ above the spin density wave transition, *Proc. Natl. Acad. Sci.* **108**, 6878 (2011).

[39] S. Graser, T. A. Maier, P. J. Hirschfeld, and D. J. Scalapino, Near-degeneracy of several pairing channels in multiorbital models for the Fe-pnictides, *New J. Phys.* **11**, 025016 (2009).

[40] J. Fink et al., Electronic structure studies of $BaFe_2As_2$ by angle-resolved photoemission spectroscopy, *Phys. Rev. B* **79**, 155118 (2009).

[41] Z. R. Ye, Y. Zhang, M. Xu, Q. Q. Ge, F. Chen, J. Jiang, B. P. Xie, J. P. Hu, and D. L. Feng, Phosphor induced significant hole-doping in ferropnictide superconductor $BaFe_2(As_{(1-x)}P_x)_2$, *Phys. Rev. B* **86**, 035136 (2012).

[42] D. Swain, S. Ghosh, K. Bera, S. Friedemann, H. Ghosh, A. Roy, and S. D. Das, Possible Raman signature of broken symmetry states near the quantum critical point in P doped $BaFe_2As_2$: Experiment and theory, *Phys. C Supercond. Its Appl.* **606**, 1354211 (2023).

[43] Y. Liu, Aliovalent ion-doped $BaFe_2As_2$: Single crystal growth and superconductivity, *Phys. C* **470**, 513 (2010).

[44] M. Neupane et al., Electron-hole asymmetry in the superconductivity of doped $BaFe_2As_2$ seen via the rigid chemical-potential shift in photoemission, *Phys. Rev. B* **83**, 094522 (2011).

[45] Y. Zhang et al., Out-of-Plane Momentum and Symmetry-Dependent Energy Gap of the Pnictide $Ba_{0.6}K_{0.4}Fe_2As_2$ Superconductor Revealed by Angle-Resolved Photoemission Spectroscopy, *Phys. Rev. Lett.* **105**, 117003 (2010).

[46] K. Nakayama et al., Universality of superconducting gaps in overdoped $Ba_{0.3}K_{0.7}Fe_2As_2$ observed by angle-resolved photoemission spectroscopy, *Phys. Rev. B* **83**, 020501 (2011).

[47] K. Nakayama et al., Superconducting gap symmetry of $Ba_{0.6}K_{0.4}Fe_2As_2$ studied by angle-resolved photoemission spectroscopy, *EPL Europhys. Lett.* **85**, 67002 (2009).

[48] G. Kresse and J. Furthmüller, Efficient iterative schemes for *ab initio* total-energy calculations using a plane-wave basis set, *Phys. Rev. B* **54**, 11169 (1996).

[49] G. Kresse and D. Joubert, From ultrasoft pseudopotentials to the projector augmented-wave method, *Phys. Rev. B* **59**, 1758 (1999).

[50] P. E. Blöchl, Projector augmented-wave method, *Phys. Rev. B* **50**, 17953 (1994).

[51] J. P. Perdew, K. Burke, and M. Ernzerhof, Generalized Gradient Approximation Made Simple, *Phys. Rev. Lett.* **77**, 3865 (1996).

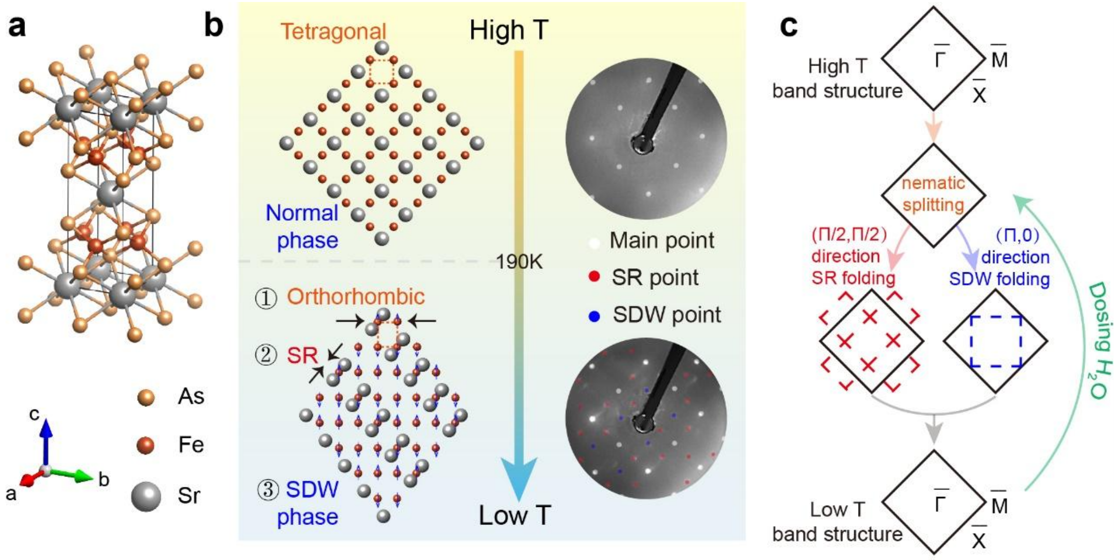

Figure 1| Phases of $SrFe_2As_2$ at high and low temperatures

(a) The room-temperature crystal structure of $SrFe_2As_2$, characterized by a tetragonal lattice. Arsenic, iron, and strontium atoms are represented by yellow, orange, and grey spheres, respectively. **(b)** The left panel illustrates the (001) surface lattice of $SrFe_2As_2$ under high and low temperatures, showcasing distinct phases at low temperatures, including ① the orthorhombic distortion, ② reconstructions involving surface Sr atoms, and ③ SDW states. The right panel presents LEED images from the pristine $SrFe_2As_2$ surface at high (300K, top) and low (80K, bottom) temperatures, captured with an electron kinetic energy of 113eV. Bragg peaks from the crystal structure are indicated by white dots, blue dots highlight the diffraction spots due to SDW ($\sqrt{2} \times \sqrt{2}$ R45°) ordering, and red dots underscore the diffraction spots arising from the (2×1) order of surface Sr reconstructions, with the coexistence of two domains. **(c)** Schematic illustration of the evolution of electronic bands in the momentum space under high and low temperatures and exposure to water.

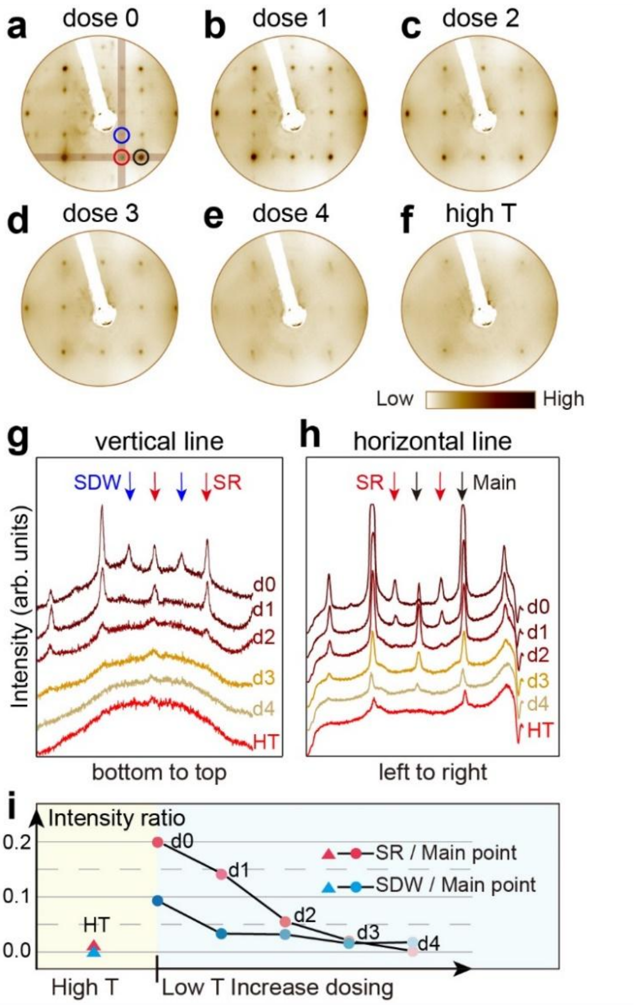

Figure 2| Evolution of the surface order after water dosage

(a-e) LEED patterns of the $SrFe_2As_2$ surface at low temperatures following increased water dosage. In **a**, diffraction spots associated with SDW order are encircled in blue, those due to Sr surface reconstruction are in red, and the Bragg points are encased in black. Throughout the water dosing and LEED measurement, the sample's temperature was maintained at 85 K. **(f)** LEED pattern from the pristine $SrFe_2As_2$ surface at room temperature (300K) for reference. **(g)** Intensity profile extracted along a vertical line in **a**, with increased water dosage; blue arrows point to the SDW diffraction spots, and red arrows to the Sr reconstruction diffraction spots. **(h)** Intensity profile along a horizontal line in **a** with increased water dosage; here, red arrows highlight the Sr reconstruction diffraction spots, and black arrows denote the lattice Bragg spots. **(i)** Variation of relative intensity ratios as a function of water dosage: the red markers illustrate the relative intensity of the surface reconstruction spots over the lattice spots, and the blue markers depict the relative intensity of the SDW spots over the lattice spots. d0: no water dose. d1-d4: water dosing 1-4 times. HT: high temperature.

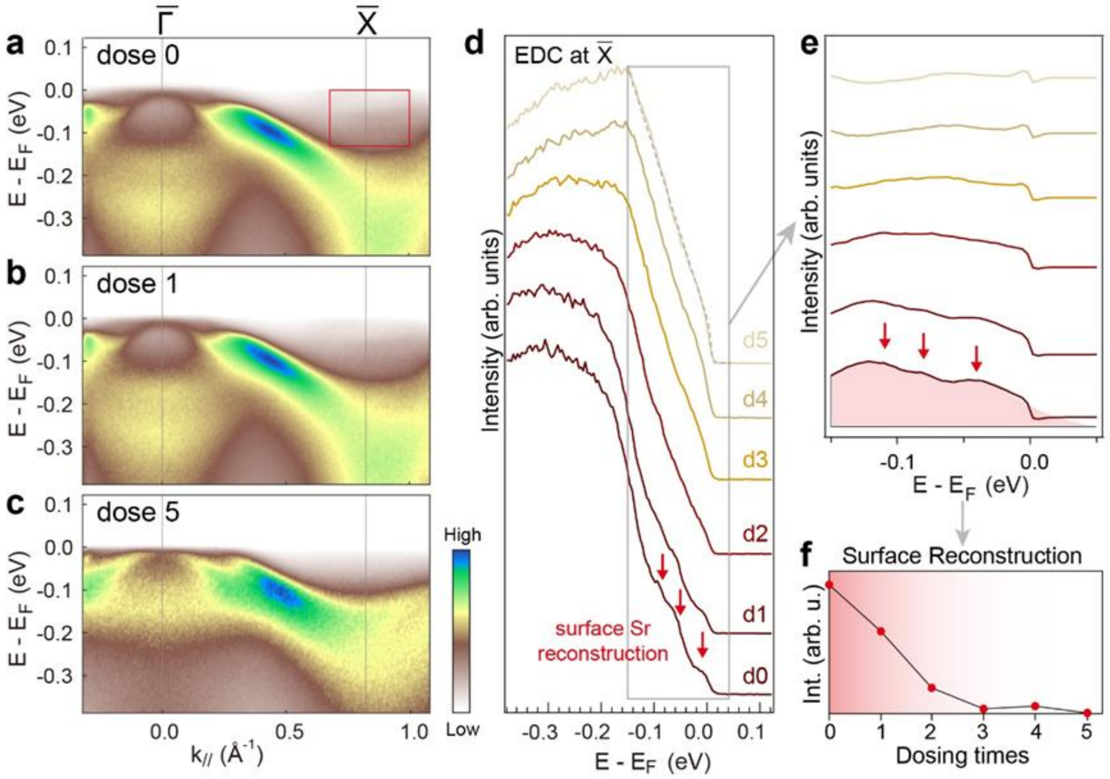

Figure 3| Evolution of the electronic structure along $\bar{\Gamma}$-$\bar{X}$ after water dosage

(a-c) Evolution of the photoemission intensity along the high-symmetry $\bar{\Gamma}$-$\bar{X}$ direction as a function of incremental water dosing. The folded bands, resultant from the 2×1 surface reconstruction, are highlighted by red rectangular box in **a**. **(d)** Plots of the energy distribution curves (EDCs) at $\bar{X}$ with different water dosages. **(e)** Plots of the EDCs post the subtraction of a linear background. The background was determined by least-squares fitting of each EDCs with a linear term plus a Fermi–Dirac function. The fitted background of d5 is overlaid in panel **d** as gray dashed lines. Red arrows label the peaks corresponding to the folded bands induced by surface reconstruction. **(f)** Depicts the variation in the integrated intensity of the EDC peaks labelled in **e** as function of water dosage. The measurement temperature was 23K. d0: no water dose. d1-d5: water dosing 1-5 times.

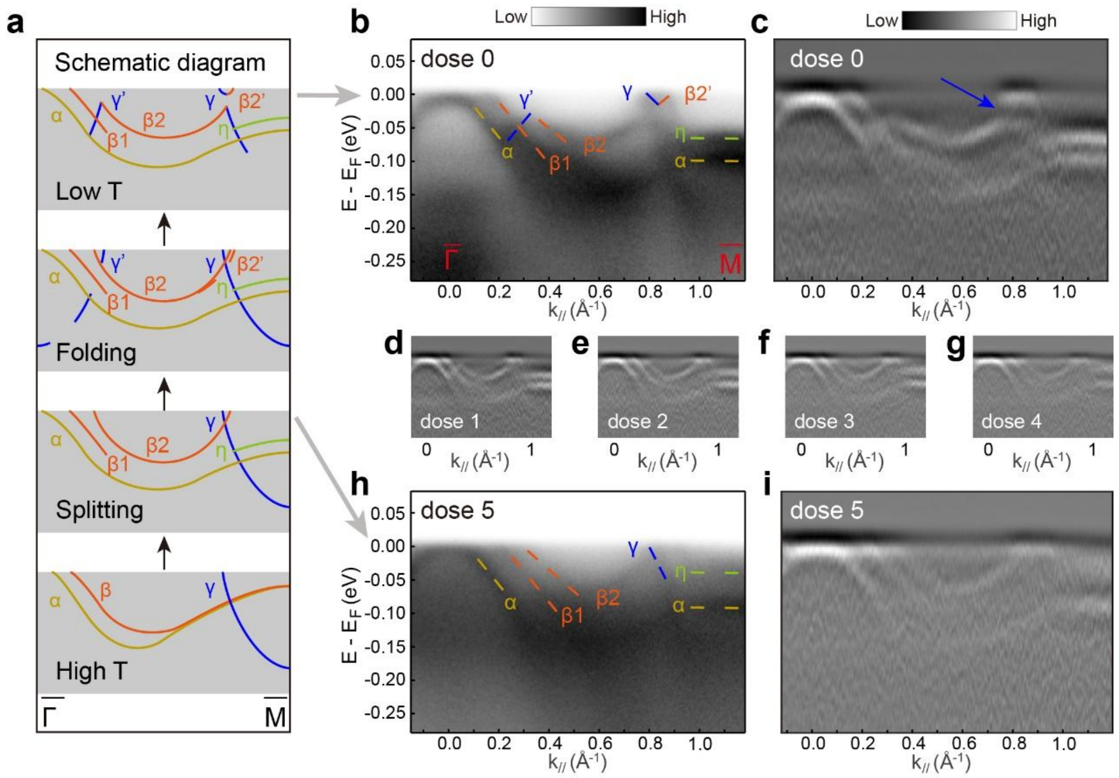

Figure 4| Evolution of the electronic structure along $\bar{\Gamma}$-$\bar{M}$ direction after water dosage

(a) Schematic of evolution of the electronic band structure along the high-symmetry $\bar{\Gamma}$-$\bar{M}$ direction with bands labelled. From bottom to top: the β band undergoes splitting due to nematic ordering, followed by folding of the γ and β bands along the $\bar{\Gamma}$-$\bar{M}$ direction with subsequent gap openings due to SDW order, finally evolving into the band structure in agreement with measured data in **b**. **(b, h)** Plot of photoemission intensity along the high-symmetry $\bar{\Gamma}$-$\bar{M}$ direction before and after dosing water. The identified bands are labelled in the same way as in **a. (c-g, i)** Plot of the second derivative of the photoemission intensity along the high-symmetry $\bar{\Gamma}$-$\bar{M}$ direction with increased water dosage. Blue arrow in **c** indicates the observed SDW gap. The measurement temperature was 20K.

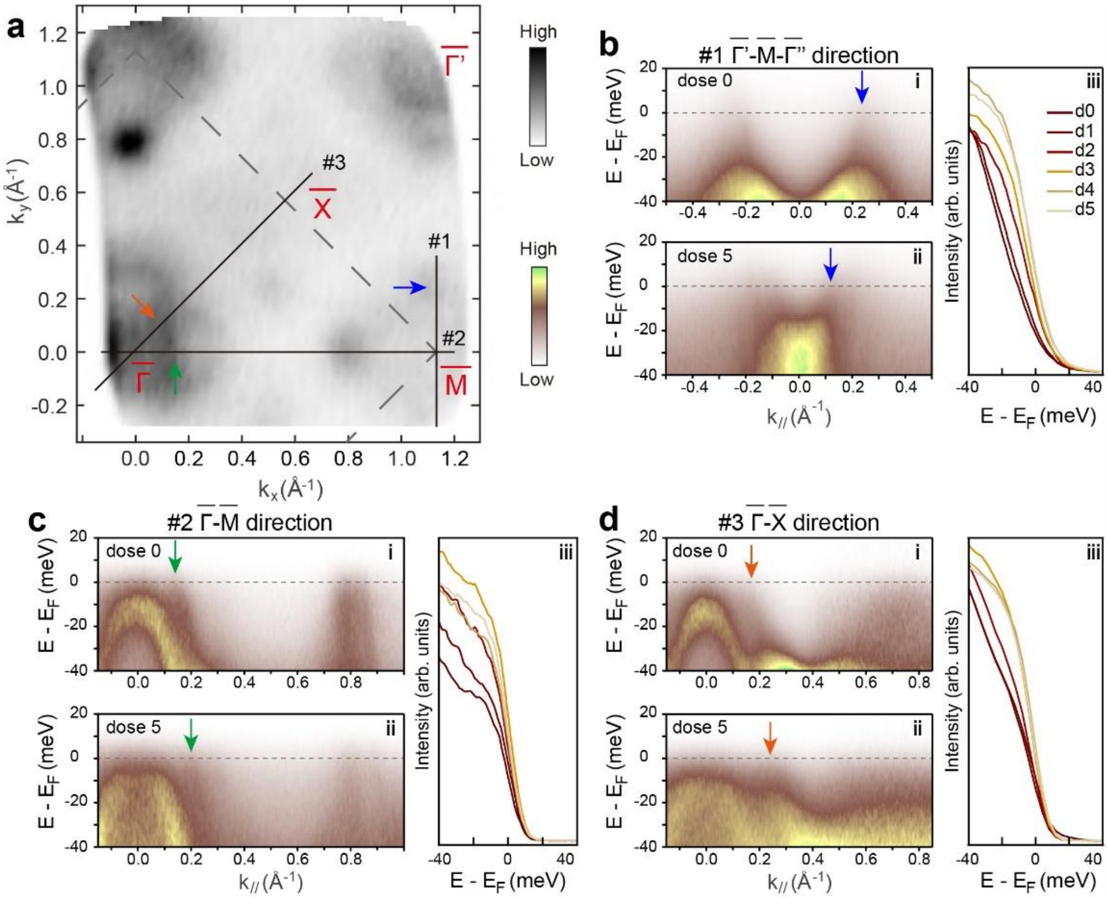

Figure 5| Evolution of the quasiparticle spectral weight of $SrFe_2As_2$ after water dosage

(a) Fermi surface map of the pristine $SrFe_2As_2$ measured at 80K, with the first Brillouin zone boundary labelled by a black dashed line. Directions for high-symmetry cuts, marked as black lines #1, #2, and #3, correspond to subsequent panels **b**, **c**, and **d**, respectively. The points where different bands cross the Fermi surface are indicated by arrows of various colors. **(b)** Plot of the photoemission intensity along the $\bar{\Gamma}' - \bar{M} - \bar{\Gamma}''$ direction with water dosing measured at 80K. **i** plot of the photoemission intensity of pristine surface, **ii** plot of the photoemission intensity of surface after 5 times of dosing. **iii** plot of the EDC at the Fermi momentum labelled by the blue arrow in panel **i** after different numbers of water dosage. **(c)** Same as **b**, but along the $\bar{\Gamma} - \bar{M}$ direction measured at 20K. Plot of the EDC at the Fermi momentum labelled by the green arrow. **(d)** Same as **b**, but along the $\bar{\Gamma} - \bar{X}$ direction measured at 23K. Plot of the EDC at the Fermi momentum labelled by the orange arrow. All spectra were normalized by the integrated weight in a high-binding-energy window.